TECHNICAL PAPER

Stiction-protected MEMS switch with low actuation voltage

Ilia V. Uvarov[1] · **Alexander N. Kupriyanov[1]**

Abstract

Commercial success of microelectromechanical systems (MEMS) switches is limited by several issues. A high actuation voltage requires special circuitry solutions that increase size and cost of the switch. Another problem is the lack of reliability due to the stiction phenomenon. This paper presents a single-pole double-throw MEMS switch with electrostatic actuation and resistive contact. The device is based on an aluminum beam suspended by the torsion springs over the driving and signal electrodes. The design provides the pull-in voltage as low as 4.9 V. At the same time, the switch is equipped with the mechanism that protects it from stiction. The device is able to operate in the passive and active opening regimes. Recovery of the device after stiction in the hot switching conditions is demonstrated. In the cold mode, stiction is not observed at the transmitted DC power up to 25 mW. The resonant properties and response time of the switch are investigated. The on-resistance and the lifecycle are discussed. The proposed design is characterized by the high mechanical reliability. The main reason of failure is an increase of the on-resistance because of carbon accumulation on the platinum contacts.

1 Introduction

In recent decades, rapid development of wireless communications has sparked a keen interest in microelectromechanical switching devices (Rebeiz et al. 2013). MEMS switches combine the advantages of semiconductor switches and electromechanical relays. They have small dimensions of several cubic millimeters, relatively low switching time of about 10 μs and near zero DC power consumption. At the same time, they demonstrate low on-resistance (less than 1 Ω) and superior RF performance (Rebeiz 2003). A significant plus of the MEMS switches is the integration capability. They are mostly based on surface micromachining, which allows fabrication together with other electronic components on a wide range of substrates including Si (Dai and Chen 2006), GaAs (Zheng et al. 2005) and glass (Zhang et al. 2018). Such characteristics make MEMS switches attractive for use in 5G mobile communications (Shekhar et al. 2018), reconfigurable antennas (Haupt and Lanagan 2013; Haider et al.

2013), satellite switching networks (Daneshmand and Mansour 2011) and other applications. In addition, the simplest logic devices (Chakraborty and Bhattacharyya 2010; Tsai et al. 2008) and memory cells (Lee et al. 2011; Chua et al. 2014) based on MEMS switches are demonstrated. MEMS switches are getting closer and closer to replacing bulky and slow electromechanical relays, as well as solid-state switches with poor performance at higher frequencies (more than 10 GHz).

A key element of the MEMS switch is a movable beam that comes in contact with the signal electrode and closes the electrical circuit. Several principles driving the beam motion are implemented: electrostatic (Zareie and Rebeiz 2014; Patel and Rebeiz 2011), piezoelectric (Sinha et al. 2012; Park et al. 2006), thermal (Zolfaghari et al. 2018; Cheng et al. 2014) and magnetic (Schiavone et al. 2014). Electrostatic actuation is the most popular, because it provides low power consumption, high switching speed, simple fabrication and easy integration with transmission lines. The main disadvantage of the electrostatic principle is the high voltage required to close the switch. Devices that ever came to the market had an actuation voltage around a few tens of volt (Happich 2018; Maciel et al. 2012; Seki et al. 2013). Such switches required an external control unit generating high-voltage signals. Some products are equipped with an integrated CMOS chip that provides the actuation voltage of 80 V and requires only

✉ Ilia V. Uvarov
i.v.uvarov@bk.ru

[1] Laboratory of Micro- and Nanosystem Technology, Institute of Physics and Technology of Russian Academy of Sciences, Yaroslavl Branch, Universitetskaya 21, 150007 Yaroslavl, Russia

3.3 V DC power supply (Goggin et al. 2015). However, the presence of the built-in driver increases the dimensions, power consumption and cost of the device. Therefore, when designing the MEMS switch, much attention is paid to reducing the actuation voltage.

The actuation voltage is determined by the pull-in phenomenon occurring in the movable mechanical structure of the switch. There are three basic ways for reducing the actuation voltage: shortening the distance between the beam and the driving electrode (Lee et al. 2010, 2013); increasing the overlap area of the beam and the electrode (Kim et al. 2011; Hirata et al. 2000); reducing the stiffness of the beam (Kim et al. 2010; Peroulis et al. 2003; Xiang and Lee 2010; Ansari and Khosroabadi 2018). As a rule, all three methods are used simultaneously, but reducing the stiffness is often preferable, because it does not increase the dimensions and does not degrade the RF performance of the device. Low stiffness is typically achieved by using special shape of the beam. For instance, the switch with double crab-leg springs and the actuation voltage of about 10 V is presented by Kim et al. (2010). Peroulis et al. (2003) report the device with the pull-in voltage of 6 V, which is achieved using meander-type suspensions. Nanoelectromechanical switch based on the cantilever attached to the torsion bar is demonstrated by Xiang and Lee (2010), the actuation voltage of 5.5 V is obtained. The helical spring design together with the reduced air gap between the beam and the transmission line allow actuation at 2.2 V (Ansari and Khosroabadi 2018).

One can see that the desired level of several volts can be reached by selecting the design of the switch. However, in most cases opening of the device is carried out by the elastic force arising in the deformed beam (passive opening). As the stiffness decreases, the opening force also decreases. As a result, a switch with not sufficiently stiff beam becomes susceptible to stiction (van Spengen et al. 2003). In this paper we present the MEMS switch whose actuation voltage can be reduced to 5 V level. At the same time, the device is equipped with the active opening mechanism allowing recovery in case of stiction. This work is a continuation of our previous studies, where the design and preliminary testing of the switch were presented (Uvarov et al. 2016, 2017; Uvarov and Kupriyanov 2018). Here we briefly describe the concept and the fabrication process of the device. Then main part of the paper is devoted to the switch performance. Passive and active opening regimes are demonstrated, pull-in and recovery voltage are measured. Then the resonant properties and response time are discussed. Finally, we investigate the on-state resistance and reliability of the switch.

2 Materials and methods

SEM image of the switch is shown in Fig. 1a. The device is based on a 1-μm-thick aluminum beam attached to the anchors by the torsion suspensions. The beam has a length L of 100 μm and a width w of 8, 16, 24 or 32 μm depending on the design. The suspensions also have the thickness of 1 μm and provide the spring constant of 1.5×10^{-8} N m. The beam is reinforced with longitudinal ribs (Fig. 1b), which increase the bending stiffness and prevent deformation under the residual mechanical stress. Perforation holes of 4 μm in diameter help to speed up the removal of the sacrificial layer from under the beam. The beam plays the role of a source electrode. Gate and drain electrodes are made of 100-nm-thick Pt film deposited on 10-nm-thick Ti adhesion layer. They are placed under the each arm of the beam, so the switch has single-pole double-throw (SPDT) configuration with two symmetric output channels. Platinum contact bumps are located on the bottom side of the beam (one bump per arm, Fig. 1b). Thus, Pt–Pt contact is obtained. Previously, the switches with an air gap g between the beam and the gate electrodes of 1.0 and 1.5 μm were tested (Uvarov and Kupriyanov 2018). The pull-in voltage as low as 12 V was achieved. In order to reduce the actuation voltage further, the batch of samples with $g = 0.5$ μm is fabricated and extensively investigated in this work. The height of the contact bumps is lowered from 0.5 to 0.25 μm in order to allow the beam movement.

The switch operates in the following manner. When the driving voltage is applied to one of the gates, the beam tilts towards it under the electrostatic force. At the certain voltage called pull-in voltage (V_{PI}) it touches the drain, and the switch goes to the on-state. When the voltage is removed or reduced to pull-out level (V_{PO}), the beam returns to the initial state under the elastic force of the suspensions and turns the switch off. In case of stiction, i.e. when the elastic force is insufficient to overcome adhesion forces acting between the bump and the drain, the switch retains the on-state. In order to detach the beam from the drain, the voltage is applied to the opposite gate. At the certain voltage called recovery voltage (V_{REC}) the beam sharply tilts to the opposite direction and comes in contact with another drain, realizing the second on-state. Therefore, the design of the switch provides the mechanism, which protects the device against stiction.

The switch is fabricated using four-mask process. The main steps are shown in Fig. 2, the detailed description can be found in Uvarov et al. (2017). Structural materials are deposited by magnetron sputtering and patterned by contact UV lithography, wet etching and lift-off. The commonly used beam material is gold. However, in this work
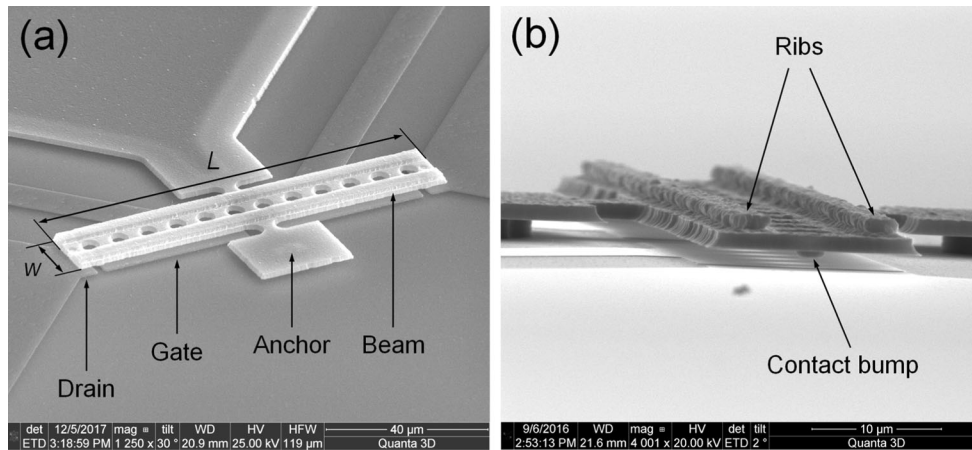
Fig. 1 SEM image of the SPDT MEMS switch with the beam width $w = 16$ μm: **a** whole design view illustrating the main parts of the device; **b** side view showing the reinforcing ribs and the contact bump

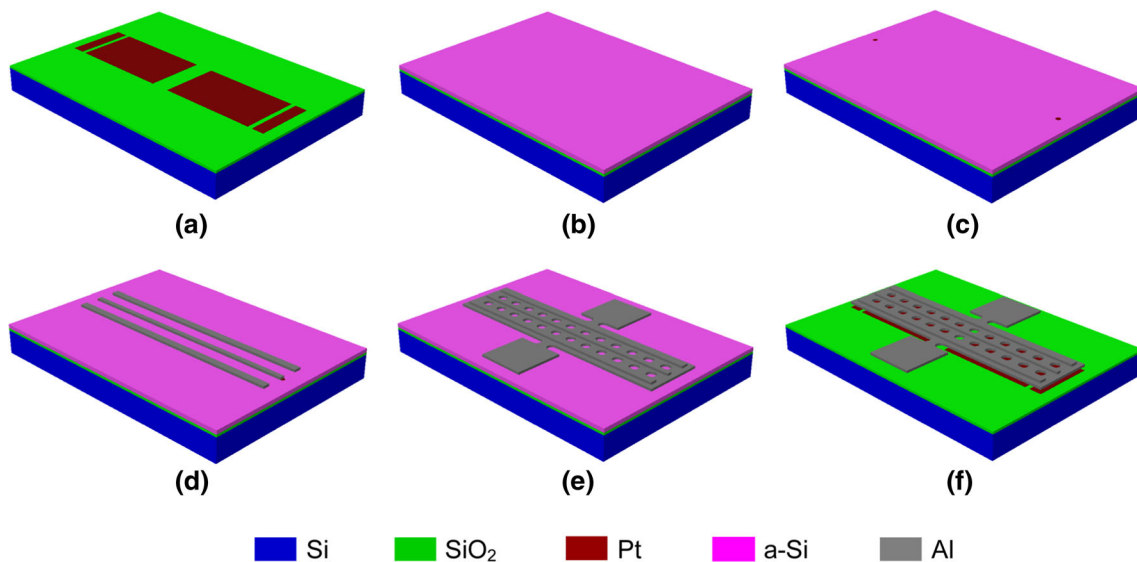**Fig. 2** Fabrication process of the switch (the device with $w = 24$ μm is shown): **a** patterning of the gate and drain electrodes; **b** deposition of the amorphous silicon (a-Si) sacrificial layer; **c** formation of the dimples in the sacrificial layer and filling them with Pt; **d** deposition of the first Al layer and patterning the ribs; **e** deposition of the second Al layer and patterning the beam and the anchors; **f** removal of the sacrificial layer by etching in SF_6 plasma

we take aluminum, because it is much cheaper, easily deposited and patterned. At the same time, electrical conductivity σ of aluminum is comparable to gold (σ_{Al} = 3.6 × 10⁷ S/m, σ_{Au} = 4.1 × 10⁷ S/m). Platinum is chosen as the contact material due to chemical inertness, relatively high hardness of 5.1 GPa and high melting temperature of 2045 K (Ekkels et al. 2009).

The switches are tested in a standard laboratory environment, unpackaged. Measurement equipment is connected to the sample as shown in Fig. 3. Driving voltage (gate voltage, V_{G1} and V_{G2}) is provided by DC power supply Agilent E3647A. Input voltage (source voltage, V_S) is applied to the beam from analog output module National Instruments (NI) PXI-6711. Output voltage (drain voltage,
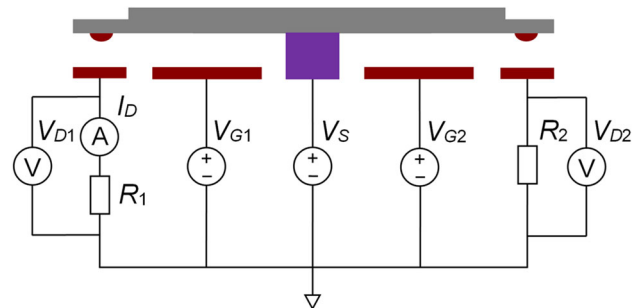

Fig. 3 Connection of the measurement equipment to the switch

V_{D1} and V_{D2}) is measured by a multifunction input/output module NI PXI-6143. Driving and output signals are

recorded by an oscilloscope PicoScope 5442B. The current I_D flowing through the switch is adjusted by load resistors R_1 and R_2. I_D is measured at the one of the channels by a multimeter Keysight 34461A. The equipment is controlled by specially written LabView software via NI PXI-GPIB module.

Resonant frequency and Q-factor of the switch are measured at a separate experimental setup. The sample is placed in a vacuum chamber providing pressure range from 10^{-2} mbar to 1 bar. The beam oscillations are excited by sinusoidal voltage applied to the gate from a waveform generator Tektronix AFG 1022. The deflection of the beam is detected by a homemade optical lever unit (Uvarov et al. 2012). Laser light (wavelength $\lambda = 0.63$ µm) passed through the optical system is focused on the beam by $20\times$ objective lens. Reflected light illuminates the position-sensitive photodetector connected to a multimeter Keysight 34461A. The resonant curve is measured automatically in the desired frequency range using LabView software.

3 Results and discussion

3.1 Pull-in, pull-out and recovery voltage

Pull-in and pull-out voltage are measured by applying a triangular waveform alternately to both gates. The voltage increases from 0 to 25 V with a rate of 40 V/s, and then decreases with the same rate. The beam is kept under the constant potential $V_S = 1$ V. Closing and opening of the channels and is detected by the sharp change of the drain voltage. It is important that the switch operates in a hot mode. To avoid accelerated damage of the contacts, the output current is limited to 0.1 mA by the load resistors $R_1 = R_2 = 10$ kΩ. Under such conditions the switch works without stiction in a passive opening regime.

The experimental values of the V_{PI} and V_{PO} are given in Table 1. Measurements are performed on ten switches of each type, taken from different points of the wafer. As expected, the wider the beam, the lower the V_{PI}. The lowest

value of 4.9 V is obtained for $w = 32$ µm. The spread of V_{PI} from sample to sample of 10–15% is associated with the thickness nonuniformity of the deposited films. The experimental V_{PI} exceeds the results of the finite element method (FEM) simulation presented in Table 1 [the modeling procedure is described by Uvarov et al. (2016)]. The reason is that the lateral dimensions of the beam are slightly smaller than the values implied in the model due to the side undercut of the patterning process. Thus, the area of the electrostatic field is reduced and the V_{PI} is increased. This effect is less pronounced on the wider beams: the discrepancy is only 2% for $w = 32$ µm. Pull-out voltage is 30–40% lower than the V_{PI}.

Increasing V_S up to 2 V causes the stiction of the switch. The stiction is overcome by applying a recovery voltage to the opposite gate. In this case, the device operates in an active opening regime. The experimental values of the V_{REC} measured at $V_S = 2$ V are shown in Table 1. V_{REC} always exceeds V_{PI}, since the voltage is applied to the capacitor with an increased air gap. In general, the samples with a wider beam have a lower recovery voltage due to the large overlap area of the electrodes. Thus, the smallest value of 14.9 V is obtained for $w = 32$ µm. However, a clear dependence of V_{REC} on w is difficult to establish due to the fact that the recovery voltage is determined not only by the switch design, but also by the adhesion force to overcome. The magnitude of this force, in turn, depends on the morphology of the contacting surfaces, the elastic and chemical properties of the contact materials, and the switching conditions (Toler et al. 2013). The fact that the stiction occurs with an increase of the output current from 10 to 20 mA indicates that the crucial role is played by the hot operation phenomena (primarily, the melting of contacts). Wear of the contacting surfaces after the test in a hot mode confirms this statement (Uvarov and Kupriyanov 2018). The values given in Table 1 should be considered as the minimum values of the recovery voltage. With a larger V_S a higher contact temperature and, consequently, a higher adhesion force are expected. Therefore, a higher voltage is required to overcome it.

3.2 Resonance frequency, Q-factor and switching time

Resonant properties of the switch are measured at the air pressure p of 0.01 mbar and 1 bar. At the atmospheric pressure the beam oscillations are excited by a sinusoidal voltage of 3 V in amplitude. In vacuum the amplitude of 0.5 V is sufficient to excite the measurable oscillations, because the air damping is reduced. The obtained resonance frequencies and Q-factors are shown in Table 2. The first vibrational mode has the torsional shape, see Fig. 4a. This mode is of primary interest, since it determines the

Table 1 Pull-in voltage V_{PI}, pull-out voltage V_{PO} and recovery voltage V_{REC} of the switches having different width of the beam w

w, µm	Model V_{PI}, V	Experiment		
		V_{PI}, V	V_{PO}, V	V_{REC}, V
8	9.8	16.1 ± 1.8	9.5 ± 2.4	19.5 ± 2.8
16	7.5	11.8 ± 0.8	7.7 ± 1.6	19.7 ± 1.6
24	5.9	7.8 ± 1.1	5.3 ± 1.5	15.7 ± 1.1
32	4.8	4.9 ± 0.6	3.6 ± 1.1	14.9 ± 2.6

Table 2 Eigenfrequencies of the first and the second vibrational modes of the beam predicted by FEM simulation, and the experimentally obtained resonant frequencies and Q-factors

w, μm	Model		Experiment				
	$f_{1,eigen}$, kHz	$f_{2,eigen}$, kHz	$f_{1,vac}$, kHz	$Q_{1,vac}$	$f_{1,atm}$, kHz	$Q_{1,atm}$	$f_{2,vac}$, kHz
8	353	619	289 ± 9	134 ± 18	287 ± 10	16 ± 2	–
16	279	579	265 ± 11	108 ± 17	264 ± 11	10 ± 2	–
24	238	554	232 ± 8	105 ± 14	229 ± 8	8 ± 1	547
32	210	530	196 ± 5	100 ± 21	194 ± 8	7 ± 1	500

The second mode is detected at the samples with w of 24 and 32 μm only

Fig. 4 Illustration of the first (**a**) and the second (**b**) vibration modes. The beam with $w = 24$ μm is shown. The other designs have the same mode shapes

(a)　　　　　　　　　　　(b)
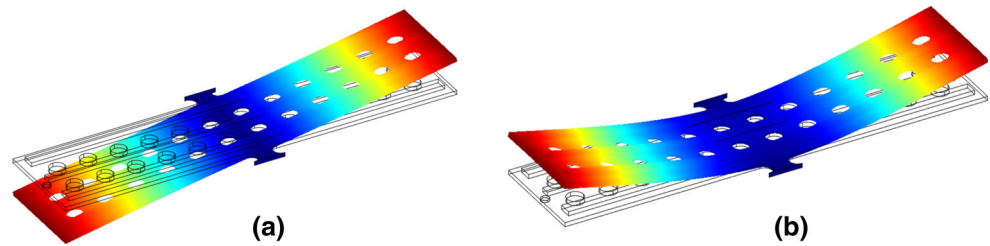
switching speed. The second (bending) mode is also detected, see Fig. 4b. The experimental setup allows finding it only in vacuum, and the oscillation amplitude is rather small in comparison with the first mode. Thus, the second resonant frequency at $p = 1$ bar and the quality factor are not measured.

The first resonance frequency f_1 is in the range from 190 to 300 kHz. It decreases with the increase of w, because the wider beam has the higher effective mass. The resonance frequencies $f_{1,vac}$ and $f_{2,vac}$ measured at $p = 0.01$ mbar are 2–20% lower than the eigenfrequencies $f_{1,eigen}$ and $f_{2,eigen}$ predicted by the FEM modeling. As in the case of the pull-in voltage, the possible reason is an undercut that reduces the lateral dimensions of the beam and the torsion springs. The frequency of the first mode $f_{1,vac}$ is 2–3 kHz lower than the value $f_{1,atm}$ obtained at $p = 1$ bar due to the higher damping at the atmospheric pressure.

The quality factor of the samples at the atmospheric pressure $Q_{1,atm}$ is in the range from 7 to 16 and decreases with increasing w. This can be explained theoretically. The main source of energy loss is the air damping. Since the gap g is much smaller than the lateral dimensions of the beam, the squeezed film damping takes place. The damping coefficient c of a rectangular beam with the length L, the width w and the thickness t, oscillating at a distance g from a fixed plate is given by the following expression (Younis 2011):

$$c = \frac{\eta L w^3}{g^3}, \tag{1}$$

where η is the viscosity of air. Q-factor of the resonator with the mass m at the n-th resonant frequency ω_n is given by:

$$Q = \frac{m\omega_n}{c}. \tag{2}$$

Substituting the expression (1) into (2), we can see that Q is inverse proportional to w^3. The decrease of the quality factor with the increase of the beam width is expected. The beam of the proposed switch has a perforation, so the expression (1) must be modified (Younis 2011). However, the correction does not change the dependence of Q on w.

An important parameter of the switch is the switching time. In the case of small damping ($Q \geq 2$) the time required to turn the switch on is determined by the following equation (Rebeiz 2003):

$$t_{on} = \frac{3.67}{2\pi f_1} \frac{V_{PI}}{V_G}, \tag{3}$$

where V_G is the gate voltage. Knowing the pull-in voltage and the resonance frequency, the response time for a given V_G can be calculated. According to the expression (3), at $V_G = V_{PI}$ the switch should go to the on-state in 2–3 μs (the values $f_{1,atm}$ for the calculations are taken from Table 2). Typically, the gate voltage of 1.3–1.4V_{PI} is used in order to ensure the actuation and to keep a reasonable voltage level (Rebeiz 2003). In these conditions the device must be switched on even faster. The time needed to turn the switch off can be estimated as follows (Kaajakari 2009):

$$t_{off} = \frac{1}{4f_1}. \tag{4}$$

According to (4), the switch should come to the off-state in 0.9–1.3 μs. The minimum duration of the switching cycle $t_{cycle} = t_{on} + t_{off}$ is less than 5 μs, that corresponds to a maximum operating frequency of 200 kHz. The experimental setup does not allow precise measurement of t_{on} and

t_{off} due to the crosstalk between the gate and the output lines. We can only say that these values not exceed 15 µs. Thus, the measurable on–off cycle duration $t_{cycle} = 30$ µs corresponds to the switching frequency of 33 kHz.

3.3 On-resistance and reliability

Reliability of the proposed switch is studied in the cyclic operation conditions. Rectangular voltage pulses are periodically applied to the gates in such a way that the channels are actuated alternately with the frequency of 2.5 Hz. Such a low frequency provides the switching cycle that is long enough for the equipment to set the required operating mode of the sample and to make all the necessary measurements during the test. The amplitude of pulses is chosen to be 30 V. This value is higher than the largest pull-in and recovery voltage (see Table 1), so it ensures the switching in both passive and active opening regimes. In contrast to the V_{PI} and V_{REC} measurement described previously, in this experiment the switch operates in a cold mode. Input voltage V_S is applied to the beam 40 ms after the channel is switched on and removed 60 ms before the channel is switched off. Thus, the hot operation and excessive wear of the contacts are avoided. All the samples are tested at $V_S = 5$ V. Unlike the hot regime, the stiction is not observed. Resistance of the both channels in the on-state R_{on} is measured at each switching cycle using the resistive divider circuit containing R_{on} and the corresponding load resistor. The experiments are performed at three levels of the current I_D flowing through the switch: 0.05, 0.5 and 5 mA.

Typical dependence of the on-resistance on the number of actuation cycles is shown in Fig. 5. At the beginning of the test the samples have R_{on} of 150–350 Ω. After a few hundred cycles the resistance starts to fluctuate between 100 and 2000 Ω. Such instability is observed for all the designs. After several thousands of cycles R_{on} sharply
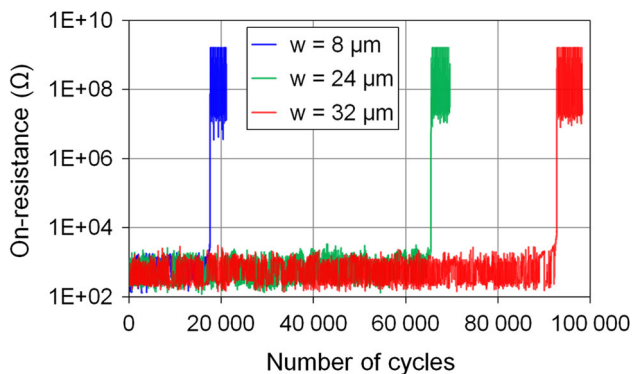
increases up to 100 MΩ that is considered as a failure. It is worth noting that the initial on-resistance at $I_D = 5$ mA is approximately two times lower and more stable than at 0.05 and 0.5 mA (see Fig. 6). The probable reason is that at the higher current the asperities of the contacting surfaces are melted easier, increasing the effective contact area which results in the lowered contact resistance.

One can see that R_{on} is rather high for ohmic MEMS switch. The resistance should be less than 5 Ω in order to provide insertion loss lower than 0.5 dB (Rebeiz 2003). R_{on} consists of two parts (Chen et al. 2007):

$$R_{on} = R_S + R_C, \tag{5}$$

where R_S is the sheet resistance of the thin metal film of the drain electrode, the beam and the signal lines, and R_C is the contact resistance caused by the current flowing through a small contact area (it is also called constriction resistance). R_S cannot be eliminated from the measurement because of practical limitations on the geometry and placement of the contact pads and connecting lines. A significant part of R_{on} comes from R_S that is estimated as 100 Ω. The instability of R_{on} is caused by R_C that includes a resistance coming from the contamination thin film between the metal contacts.

The constriction resistance for a single asperity contact is given by Holm (1967):

$$R_C = \frac{\rho}{2a}, \tag{6}$$

where ρ is the electrical resistivity and a is the radius of the contact spot. The model for a is determined by the type of asperity deformation. For a contact force F_C less than 200 µN the deformation is assumed to be elastic, and over 200 µN it is plastic (Rebeiz 2003). The contact force provided by the switch is simulated using FEM software. The dependence of F_C on the beam width is shown in Fig. 7. The maximum value of 27 µN is achieved by the device with $w = 32$ µm. Therefore, elastic deformation

Fig. 5 Dependence of the on-resistance on the number of actuation cycles for three samples having different w. Measurements are performed at $I_D = 0.5$ mA
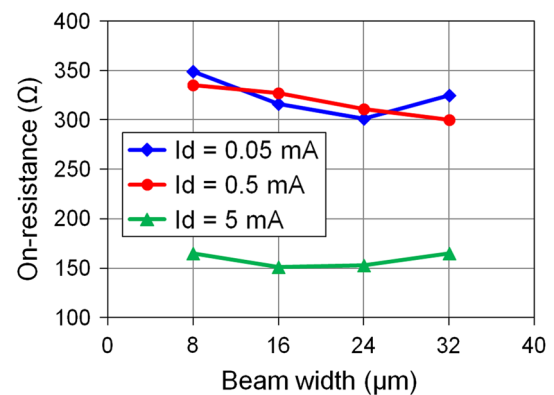

Fig. 6 Dependence of the initial on-resistance on the beam width
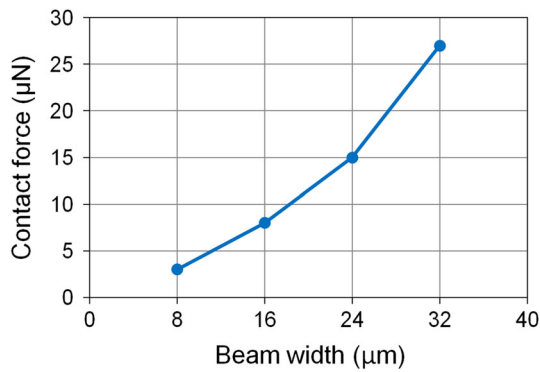
Fig. 7 Simulated dependence of the contact force at $V_G = 30$ V on the beam width

takes place, and the contact radius is calculated in accordance with the Hertz's model (Holm 1967):

$$a = \sqrt[3]{\frac{3F_C r}{4E'}}, \tag{7}$$

where r is the asperity peak radius of curvature and E' is the is the effective Hertzian modulus derived from:

$$\frac{1}{E'} = \frac{1 - v_1^2}{E_1} + \frac{1 - v_2^2}{E_2}, \tag{8}$$

where E_1, v_1 and E_2, v_2 are the Young's modulus and Poisson's ratio of the contact one and two, respectively. In

order to calculate the contact resistance, detailed information on the morphology of the contacting surfaces is required. Combination of the expressions (6) and (7) shows that R_{on} is inversely proportional to $F_C^{1/3}$. Therefore, the switch with a wider beam is expected to have smaller on-resistance. Nevertheless, R_{on} does not depend on w, see Fig. 7. Precise measurement of the contact resistance is needed to explain this result.

In order to identify the reason of the on-resistance instability and sudden resistive failure of the switch the contacting surfaces are inspected using SEM Zeiss Supra 40. A piece of adhesive tape is glued to the switch and then peeled off to flip the beam over and to make the surfaces observable. Figure 8 shows the contact bump and the drain electrode of the switch failed after 5×10^4 cycles at $I_{D-} = 0.5$ mA. Both parts have damaged areas with the lateral size of about 0.5 μm. Clusters of material are formed on the contact bump possibly due the transfer of platinum from the drain. These clusters are up to 50 nm in height. As a result of their formation, the contact area decreases leading to the increase of R_C.

Chemical composition of the damaged regions is measured by energy dispersive X-ray (EDX) analysis using the Oxford Instruments INCA x-ACT detector. Two areas of the drain electrode with the size of 0.5×0.5 μm^2 are investigated. The area 1 is located at the unaffected surface
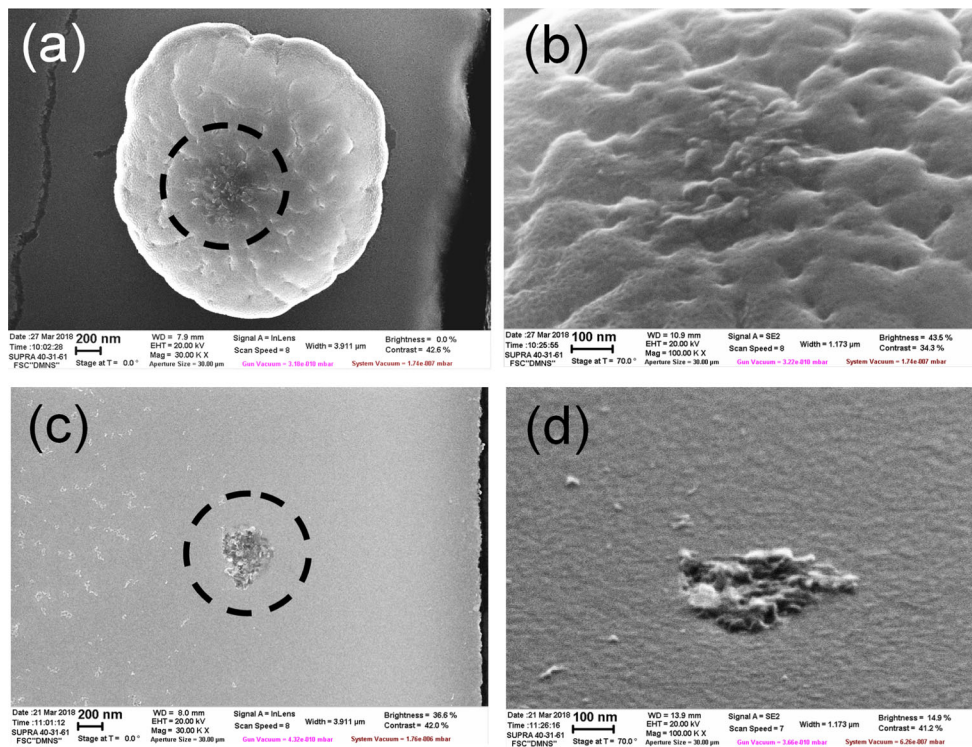

Fig. 8 SEM images of the contact bump (**a**, **b**) and the drain electrode (**c**, **d**) made after 5×10^4 cycles at $I_D = 0.5$ μA. The images **a** and **c** are taken at the angle of 90° with respect to the sample surface, the

magnification is 30,000. Black circles indicate the damaged areas. Images **b** and **d** show the close-up view of the damaged zones. The angle is 20° and the magnification is 100,000

Table 3 The results of the EDX analysis

Chemicalelement	Area 1		Area 2	
	Weight %	Atomic %	Weight %	Atomic %
C	0.82	10.66	1.20	14.41
O	0.35	3.38	0.57	5.13
Si	0.64	3.52	0.91	4.68
Pt	103.60	82.45	102.84	75.78
Total	105.41		105.53	

of the electrode, while the area 2 contains the damaged zone. Data on the chemical composition are presented in Table 3. The damaged area contains approximately 35% more carbon than the clean area. This indicates that carbon accumulates on the contacting surfaces during cycling. This phenomenon is known as contamination or frictional polymerization (Toler et al. 2013). It is widely observed at the platinum group metal contacts (Czaplewski et al. 2012; Song et al. 2013). Several methods of reducing the contamination rate are known, such as hermetic packaging (Czaplewski et al. 2012) and alloying the contact material with Au (Chen et al. 2007). With these methods the contact resistance can be reduced and the lifecycle of the switch can be increased.

It is worth noting that the area 2 contains slightly less platinum than the area 1. This is due to the transfer of Pt from the drain electrode to the contact bump. Material transfer increases the amount of oxygen and silicon in the X-ray spectrum of the sample, because the thinner Pt layer is more transparent for X-ray radiation generated in the SiO_2 isolation layer.

Lifetime of the switch is limited by the sharp increase of R_{on} and varies from 2×10^3 to 5×10^4 operation cycles. The samples with the narrowest beam fail with the least number of cycles at the all I_D values. To all appearance, the extremely low contact force $F_C = 3$ μN is insufficient to break the continuously growing contamination film. Switches with $w = 24$ μm typically demonstrate the longest lifecycle. At $I_D = 5$ mA the lifecycle is slightly lower than at 0.05 and 0.5 mA. It is connected with the higher temperature of the contact spot that caused intensified wear of the contacting surfaces. In general, the obtained data correspond to the endurance of the switches with the Pt–Pt contact available in the literature (Chen et al. 2007; Song et al. 2013). The stiction is not observed even at the current of 5 mA, which corresponds to the transmitted power of 25 mW. The higher power is not applied because of the limitations of the experimental setup. However, the obtained value of 25 mW is not the limit of the switch capabilities. Further we plan to test the device for transmission of higher power signals.

4 Conclusions

Electrostatically actuated MEMS switch with low pull-in voltage and protection against stiction is presented in this paper. Several designs having different width of the beam are investigated. The switch with the widest beam has the pull-in voltage less than 5 V, that is significantly lower than the driving voltage of the commercially available products. Response time of the device is at the standard level, the switching time does not exceed 15 μs. The device is tested in a DC regime in hot and cold modes. Hot switching leads to stiction, which can be overcome by applying a recovery voltage to the opposite gate. The recovery voltage is higher than the pull-in voltage, it has a value of 15–20 V. However, the active opening regime is characterized by low power consumption, since no voltage is required to maintain the closed state. This regime is attractive for stand-alone systems, including wireless communication devices. In the cold switching conditions, no stiction is observed at the transmitted power up to 25 mW. The switch has a lifecycle from 2×10^3 to 5×10^4 actuation cycles, that is limited by a sharp increase of the on-resistance. The reason is the accumulation of carbon on the platinum contacts. The design with the narrowest beam has the lowest lifecycle, since it provides the lowest contact force. Thus, the probability of stiction failure is minimized due to the active opening mechanism. The main cause of malfunction is the degradation of the contacts. Solution of the contamination problem will significantly increase the reliability of the device. The proposed design can also be used in capacitive MEMS switches.

References

Ansari HR, Khosroabadi S (2018) Design and simulation of a novel RF MEMS shunt capacitive switch with a unique spring for Ka-band application. Microsyst Technol. https://doi.org/10.1007/s00542-018-3989-9

Chakraborty S, Bhattacharyya TK (2010) Development of a surface micro-machined binary logic inverter for ultra-low frequency MEMS sensor applications. J Micromech Microeng 20:105026

Chen L, Lee H, Guo ZJ, McGruer NE, Gilbert KW, Mall S, Leedy KD, Adams GG (2007) Contact resistance study of noble metals and alloy films using a scanning probe microscope test station. J Appl Phys 102:074910

Cheng P, Zhang Y, Mao S, Wang H, Ding G, Zhang C, Dai X, Zhao X (2014) Novel electro-thermal latching micro-switch based on Ni/electrophoretic polymer micro-cantilevers. J Micromech Microeng 24:125015

Chua GL, Singh P, Soon BW, Liang YS, Jayaraman KG, Kim TT-H, Singh N (2014) Molecular adhesion controlled microelectromechanical memory device for harsh environment data storage. Appl Phys Lett 105:113503

Czaplewski DA, Nordquist CD, Dyck CW, Patrizi GA, Kraus GM, Cowan WD (2012) Lifetime limitations of ohmic, contacting RF MEMS switches with Au, Pt and Ir contact materials due to accumulation of 'friction polymer' on the contacts. J Micromech Microeng 22:105005

Dai C-L, Chen J-H (2006) Low voltage actuated RF micromechanical switches fabricated using CMOS-MEMS technique. Microsyst Technol 12:1143–1151

Daneshmand M, Mansour RR (2011) RF MEMS satellite switch matrices. IEEE Microw Mag 12:92–109

Ekkels P, Rottenberg X, Puers R, Tilmans HAC (2009) Evaluation of platinum as a structural thin film material for RF-MEMS devices. J Micromech Microeng 19:065010

Goggin R, Fitzgerald P, Stenson B, Carty E, McDaid P (2015) Commercialization of a reliable RF MEMS switch with integrated driver circuitry in a miniature QFN package for RF instrumentation applications. In: 2015 IEEE MTT-S International Microwave Symposium. https://doi.org/10.1109/MWSYM.2015.7166959

Haider N, Caratelli D, Yarovoy AG (2013) Recent developments in reconfigurable and multiband antenna technology. Int J Antenn Propag 2013:869170

Happich J (2018) MEMS goes into 10A power switches. eeNews Europe. http://www.eenewseurope.com/news/mems-goes-10a-power-switches. Accessed 28 Sept 2018

Haupt RL, Lanagan M (2013) Reconfigurable antennas. IEEE Antennas Propag Mag 55:49–61

Hirata A, Machida K, Kyuragi H, Maeda M (2000) A electrostatic micromechanical switch for logic operation in multichip modules on Si. Sens Actuators 80:119–125

Holm R (1967) Electric contacts: theory and application. Springer, Berlin

Kaajakari V (2009) Closed form expressions for RF MEMS switch actuation and release time. Electron Lett 45:149–150

Kim J-M, Lee S, Park J-H, Baek C-W, Kwon Y, Kim Y-K (2010) Electrostatically driven low-voltage micromechanical RF switches using robust single-crystal silicon actuators. J Micromech Microeng 20:095007

Kim M-W, Song Y-H, Yoon J-B (2011) Modeling, fabrication and demonstration of a rib-type cantilever switch with an extended gate electrode. J Micromech Microeng 21:115009

Lee T-H, Bhunia S, Mehregany M (2010) Electromechanical computing at 500 °C with silicon carbide. Science 329:1316–1318

Lee SW, Park SJ, Campbell EEB, Park YW (2011) A fast and low-power microelectromechanical system-based non-volatile memory device. Nat Commun 2:220

Lee JO, Song T-H, Kim M-W, Kang M-H, Oh J-S, Yang H-H, Yoon J-B (2013) A sub-1-volt nanoelectromechanical switching device. Nat Nanotechnol 8:36–40

Maciel J, Majumder S, Lampen J, Guthy C (2012) Rugged and reliable ohmic MEMS switches. In: 2012 IEEE/MTT-S international microwave symposium digest. https://doi.org/10.1109/MWSYM.2012.6258368

Park J-H, Lee H-C, Park Y-H, Kim Y-D, Ji C-H, Bu J, Nam H-J (2006) A fully wafer-level packaged RF MEMS switch with low actuation voltage using a piezoelectric actuator. J Micromech Microeng 16:2281–2286

Patel CD, Rebeiz GM (2011) RF MEMS metal-contact switches with mN-contact and restoring forces and low process sensitivity. IEEE Trans Microw Theory Techn 59:1230–1237

Peroulis D, Pacheco SP, Sarabandi K, Katehi LPB (2003) Electromechanical considerations in developing low-voltage RF MEMS switches. IEEE Trans Microw Theory Techn 51:259–270

Rebeiz GM (2003) RF MEMS: theory, design, and technology. Wiley, New Jersey

Rebeiz GM, Patel CD, Han SK, Ko C-H, Ho KMJ (2013) The search for a reliable MEMS switch. IEEE Microw Mag 14:57–67

Schiavone G, Desmulliez MPY, Walton AJ (2014) Integrated magnetic MEMS relays: status of the technology. Micromachines 5:622–653

Seki T, Yamamoto J, Murakami A, Yoshitake N, Hinuma K, Fujiwara T, Sano K, Matsushita T, Sato F, Oba M (2013) An RF MEMS switch for 4G Front-Ends. In: 2013 IEEE MTT-S International Microwave Symposium Digest (MTT). https://doi.org/10.1109/mwsym.2013.6697501

Shekhar S, Vinoy KJ, Ananthasuresh GK (2018) Low-voltage high-reliability MEMS switch for millimeter wave 5G applications. J Micromech Microeng 28:075012

Sinha N, Jones TS, Guo Z, Piazza G (2012) Body-biased complementary logic implemented using AlN piezoelectric MEMS switches. J Microelectromech Syst 21:484–496

Song Y-H, Kim M-W, Lee JO, Ko S-D, Yoon J-B (2013) Complementary dual-contact switch using soft and hard contact materials for achieving low contact resistance and high reliability simultaneously. J Microelectromech Syst 22:846–854

Toler BF, Coutu RA, McBride JW (2013) A review of micro-contact physics for microelectromechanical systems (MEMS) metal contact switches. J Micromech Microeng 23:103001

Tsai C-Y, Kuo W-T, Lin C-B, Chen T-L (2008) Design and fabrication of MEMS logic gates. J Micromech Microeng 18:045001

Uvarov IV, Kupriyanov AN (2018) Investigation of characteristics of electrostatically actuated MEMS switch with an active contact breaking mechanism. Russ Microlectron 47:307–316

Uvarov IV, Naumov VV, Amirov II (2012) Resonance properties of multilayer metallic nanocantilevers. Proc SPIE 8700:87000S-1

Uvarov IV, Naumov VV, Koroleva OM, Vaganova EI, Amirov II (2016) A low actuation voltage bistable MEMS switch: design, fabrication and preliminary testing. Proc SPIE 10224:102241A

Uvarov IV, Naumov VV, Kupriyanov AN, Koroleva OM, Vaganova EI, Amirov II (2017) Resistive contact MEMS switch in a "hot" operation mode. J Phys Conf Ser 917:082001

van Spengen WM, Puers R, de Wolf I (2003) On the physics of stiction and its impact on the reliability of microstructures. J Adhesion Sci Technol 17:563–582

Xiang W, Lee C (2010) Nanoelectromechanical torsion switch of low operation voltage for nonvolatile memory application. Appl Phys Lett 96:193113

Younis MI (2011) MEMS linear and nonlinear statics and dynamics. Springer Science + Business Media LLC, Boston

Zareie H, Rebeiz GM (2014) Compact high-power SPST and SP4T RF MEMS metal-contact switches. IEEE Trans Microw Theory Techn 62:297–305

Zhang X, Adelegan OJ, Yamaner FY, Oralkan O (2018) A fast-switching (1.35-μs) low-control-voltage (2.5-V) MEMS T/R switch monolithically integrated with a capacitive micromachined ultrasonic transducer. J Microelectromech Syst 27:190–200

Zheng W-B, Huang Q-A, Liao X-P, Li F-X (2005) RF MEMS membrane switches on GaAs substrates for X-band applications. J Microelectromech Syst 14:464–471

Zolfaghari P, Arzhang V, Zolfaghari M (2018) A low loss and power efficient micro-electro-thermally actuated RF MEMS switch for low power and low loss applications. Microsyst Technol 24:3019–3032